Biointerface Research in Applied Chemistry
Open-Access Journal (ISSN: 2069-5837)

Article
Volume 13, Issue 6, 2023, 557
https://doi.org/10.33263/BRIAC136.557

Theoretical and Experimental Studies of Lentisk Leaf Extract as Green Corrosion Inhibitor for Iron in Chloride Media

Mohammed Barbouchi [1,*], Bouchra Benzidia [2], Adib Ghaleb [3], Adnane Aouidate [4], Mostafa El Idrissi [4], M'barek Choukrad [1]

[1] Laboratory of Molecular Chemistry and Natural Substances, Department of Chemistry, Faculty of Sciences, Moulay Ismail University, B.P 11201 Zitoune, Meknes-Morocco; med.barbouchi@gmail.com (M.B.); mostafa.elidrissi@hotmail.fr (M.E.); mchoukrad@yahoo.fr (M.C.);
[2] Laboratory of Organic Chemistry, Catalysis and Environment, Department of Chemistry, Faculty of Sciences, Ibn Tofail University, BP 133, 14000 Kenitra, Morocco; benzidia1511@gmail.com (B.B.);
[3] Laboratory of Analytical and Molecular Chemistry (LCAM), Department of Chemistry, Faculty Polydisciplinary Safi, Cadi Ayyad University, Safi, 46030, Morocco; adib.ghaleb@gmail.com (A.G.);
[4] Institute of Organic and Analytical Chemistry (ICOA), University of Orleans, UMR-CNRS 7311, BP 6759, rue de Chartres 45067 Orleans Cedex 2, France; a.aouidate@hotmail.fr (A.A.);
* Correspondence: med.barbouchi@gmail.com (M.B.);

Scopus Author ID 57202071850
8202102000 (M.E.)
57213990052 (M.C.)
Received: 25.10.2022; Accepted: 13.01.2023; Published: 24.02.2023

Abstract: This study aims at studying the inhibition impact of the ethanol extract of Lentisk leaf (EELL) as a green inhibitor of iron corrosion in chloride media. The experimental study was conducted by Potentiodynamic polarization (PDP) methods and electrochemical impedance spectroscopy (EIS). Also, the GC/MS was used to identify the major components of the EELL, and the Fourier transform infrared spectroscopy (FT-IR), ultraviolet-visible (UV-Vis), and scanning electron microscopy coupled with energy dispersive X-ray spectroscopy (SEM/EDX) techniques were employed to analyze the iron surface. Moreover, to investigate the adsorption action of EELL over the iron surface, the theoretical simulations based on the MD (molecular dynamics) and DFT (density functional theory) were done. The main constituents of EELL are palmitic acid (27.5%), then stearic acid (22.5%), and 6β-hydroxy 21-acetyloxy budesonide (22.2%). Results provided by EIS analysis demonstrated 82% efficiency for 3% NaCl solution protected by 100 ppm of the EELL. The Tafel polarization studies illustrated the suppression of the cathodic reaction in a 3% NaCl medium filled with the EELL. In addition, PDP curves indicated that EELL behaves as a cathodic inhibitor. Moreover, the results of theoretical modeling studies supported the adsorption of EELL molecules on the target metal substrate.

Keywords: Lentisk; Green inhibitor; Iron; 3% NaCl; DFT; MD simulation.

1. Introduction

As a complex natural phenomenon, corrosion has always been a significant industrial problem. Despite scientific and technological advances developed and accumulated over the past decades, corrosion still causes great damage and affects many areas [1]. This industrial disease can take various forms ranging from simple uniform corrosion to more complex aspects encountered in harsh industrial environments.

One effective/economic approach for lowing the metal (iron and its alloys) dissolution rate during electrolyte (acidic, neutral, or alkaline) treatment is the application of organic and/or inorganic corrosion inhibitors [2,3]. However, most corrosion inhibitors are known for their toxicity [4]. Indeed the great challenges of the scientists have been to develop inhibitors, their choice always being the result of a compromise which is at the same time technical, effective, and often now eco-friendly and efficient [5].

In recent years, being low-cost, eco-friend, biodegradable, renewable, available, non-toxic, and readily obtainable, the extracts from different parts (flowers, leaves, seeds, fruits, and twigs) of plants as one of the most popular corrosion inhibitors [6,7]. The researchers have made several attempts to study the corrosion inhibition properties of sustainable inhibitors on the metal and alloys in acidic and neutral solutions. They have revealed that the green inhibitors extracted from different parts of the plant exhibit inhibition toward metal and alloy corrosion [8–18]. Notwithstanding the good results of sustainable corrosion inhibitors demonstrated that many powerful green inhibitors can offer superior corrosion inhibition in the acidic (H_2SO_4 or HCl) electrolytes and are not always effective enough to control corrosion in neutral (NaCl) electrolytes [19]. The efficiency of these green inhibitors of corrosion is related to the abundant chemical constituents with the functional groups (-SH, -OH, -COOH, -NH_2, etc.) containing S, O, or N atoms, which are centers for the adsorption process. The double bonds and aromatic rings and the size of the inhibitor molecules chains also favor the adsorption on the surface [5,18].

Given the lack of data on using Lentisk extracts as a source of corrosion inhibitor in a neutral chloride medium. This is the first time ethanol extract of Lentisk extract is applied as a green corrosion inhibitor for iron in chloride media. Lentisk is a spontaneous plant widely distributed in semi-arid areas of the Mediterranean region [20]. In addition, Lentisk is a plant known for its medicinal properties since ancient times. Its different parts contain various medically important chemical components [21,22]. It has several properties such as antimicrobial [23,24], antioxidant [25–27], antibacterial [28], anticancer and anti-inflammatory [29,30], antifungal [31,32], antidiabetic and antitumor [33,34]. These advantages, being low-cost, eco-friendly, biodegradable, available, and readily obtainable, have made the extract of Lentisk leaf interesting corrosion inhibitors.

In this work, an experimental and theoretical investigation has been performed to evaluate the corrosion inhibition property of the ethanol extract of Lentisk leaf (EELL) on iron in a neutral chloride solution. The inhibition performance was provided via PDP and EIS. Surface characterizations, including SEM, EDX, UV-Vis, and FT-IR, were conducted. Furthermore, the theoretical modeling was carried out using MD and DFT techniques to explore the adsorption of the inhibitor molecules over the metal surface.

2. Materials and Methods

2.1. Extract preparation.

Lentisk (*Pistacia lentiscus* L.) was collected from Moulay Idriss Zerhoun, a town in northern Morocco. The Geographical coordinate is N 33° 50' 50.4636” ; W 5° 19' 0.3972”. The leaves of Lentisk were air-dried for 20 days at room temperature.

The dried powder leaves (50 g) of Lentisk were extracted with 400 mL ethanol absolute (obtained from Sigma-Aldrich) in a soxhlet apparatus for 8 hours. The crude extract obtained from Lentisk leaf was filtered and evaporated. The obtained ethanolic extract was analyzed by

Clarus SQ 8C Gas chromatograph coupled with a mass spectrometer (GC/MS) from PerkinElmer, equipped with a Rxi-5MS capillary column (30 m x 0.25 mm x 0.25 µm). For the analysis process, we adopted the method used in previous works [35,36].

2.2. Electrolyte and sample preparation.

The composition of working electrode disk (with a surface area of 1 cm^2) and iron coupons (having dimensions 2.5 × 1 × 0.1 cm^3) employed in this study was as follows (wt %): Mn(0.514), Si(0.201), C(0.157), S(0.009), P(0.007), and remainder Fe. Before every experiment, the surface of iron was rubbed with several grades of SiC abrasive papers (80, 220, 400, 600, 1000, 1200, and 2000), and then the iron surface was washed thoroughly via distilled water and acetone.

The Neutral chloride electrolyte (3% NaCl) was achieved by dissolving NaCl Merck in double distilled water. Finally, different amounts of EELL powder were dissolved in the prepared electrolyte to obtain solutions with concentrations ranging of inhibitor from 25 ppm to 100 ppm.

2.3. Electrochemical measurements.

The electrochemical measurements have been achieved by a potentiostat-galvanostat SP-200 (Biologic Science Instruments). Three-electrode cells with an iron-working electrode, a platinum electrode as counter-electrode, and XR300/XR310 reference electrode Ag/AgCl. Prior to use, the working electrode is maintained prior to immersion in free corrosion potential for 30 minutes. PDP was recorded by scanning the potential from -250 to +250 mV versus OCP with the scanning speed is 1 mV/s.

The inhibition efficiency (η_{PDP} (%)) be computed by the following Equation (1):

$$\eta_{PDP}(\%) = [1 - \frac{i_{corr}}{i^{\circ}_{corr}}] \times 100 \quad (1)$$

where i°_{corr} and i_{corr} are corrosion current densities values without and with inhibitors, respectively.

The plot of the EIS diagrams was conducted on a wave at a frequency range between 100 KHz and 10 mHz and a potential amplitude of 10 mV on a steady-state open-circuit potential. As regards the inhibition efficiency (η_{EIS} (%)) was computed by Equation (2):

$$\eta_{EIS}(\%) = [1 - \frac{R_P}{R_{P(inh)}}] \times 100 \quad (2)$$

where the R_p and $R_{p(inh)}$ represent the polarization resistance in the absence and presence of the inhibitor, respectively.

The electrochemical parameters from the polarization curves and electrochemical impedance diagrams are determined via EC-Lab software 11.26.

2.4. Surface characterizations.

FT-IR and UV-Vis spectra were recorded for assessment of the EELL constituents and formed film on the metal surface. The functional groups of the EELL were identified in the frequency range between 400 and 4000 cm^{-1} using a JASCO-4100 FT-IR spectrometer. The UV-Vis spectroscopy was operated using a SHIMADZU UVmin-1240 scanning spectrophotometer (wavelength limited between 190 and 800 nm).

The surficial film morphology/microstructure of the samples (1 cm × 1 cm) was examined by SEM/EDX (scanning electron microscopy / the Energy Dispersive X-ray microanalysis) using the Quanta 450 FEG from the FEI.

2.5. Global quantum chemical descriptors (GQCDs).

The molecular structures of EELL compounds were fully equilibrated in the gas phase by means of DFT (Density functional theory) with the hybrid function of B3LYP (Becke three-parameters Lee, Yang, and Parr), that is DFT/B3LYP method, and basis sets 6-311G** as triple basis functions in Gaussian 09 software. Afterward, the DFT study was done in an aqueous medium using SCRF theory based on the PCM model. Indeed, the electronic inhibitors properties analyzed here include several theoretical indices: frontier molecular orbitals (E_{LUMO} and E_{HOMO}), energy band gap (ΔE_{gap}), fraction of electron transfer (ΔN), electron affinity (E_A), ionization potential (I_P), electronegativity (χ), hardness (η), electrophilicity index (ω), nucleophilicity index (N) and softness (σ). The computational parameters can be calculated from the values of E_{HOMO} and E_{LUMO} using the following relations given below [37–39].

$$\Delta E_{gap} = E_{LUMO} - E_{HOMO} \quad (1)$$

$$\Delta N_{110} = \frac{\phi - \chi_{inh}}{2(\eta_{Fe} + \eta_{inh})} \quad (2)$$

The function ∅ is the electronegativity of the metal surface; for Fe (110) surface it gives 4.82 eV.

$$\chi = \frac{I_P + E_A}{2} \quad (3)$$

$$\eta = \frac{I_p - E_A}{2} \quad (4)$$

where the $I_p = -E_{HOMO}$ and $E_A = -E_{LUMO}$.

$$\omega = \frac{\mu^2}{2\eta} \quad (5)$$

Where the electronic chemical potential $\mu = ((E_{LUMO} + E_{HOMO})/2)$

$$N = E_{HOMO}(Nucleophile) - E_{HOMO}(TCE) \quad (6)$$

The tetracyanoethylene (*TCE*) is taken as a reference because of its lower E_{HOMO} in a large series of molecules.

$$\sigma = \frac{1}{\eta} \quad (7)$$

2.6. Molecular dynamics simulations.

In order to investigate at an atomic scale the adsorption of green compounds that exist in EELL on the metal substrate under a variety of conditions to aid in the interpretation of the experimental findings, we carried out the MD simulations that have been adopted as effective and authentic techniques.

The Forcite module performed in Materials Studio software was employed to estimate the nature of the interaction between the studied inhibitors (Table 5) and the iron sorbent [40]. For this purpose, the Fe crystal was imported, then cleaved alongside the (110) plane, and a slab of 5 Å was utilized. The surface of Fe (110) was relaxed by minimizing its energy by

employing the smart minimizer method. The Fe (110) surface was also enlarged to a (10 × 10) supercell to envisage a wide surface for the interaction of studied inhibitors. Then, a vacuum slab of 30 Å thickness was constructed above the Fe (110) plane. A supercell composing of 500 H_2O, 5 NaCl molecules were added, and finally, we created the molecules of the tested inhibitors. The simulation was achieved via a simulation box in the NVT canonical ensemble at 298 K with a time step of 0.1 fs and simulation time of 2000 ps carried out at 298 K, NVT ensemble, as well as COMPASS force field [41]. In the simulation system, the interactions and binding energies of the EELL inhibitor with the Fe (110) surface were estimated by using the following equations [42,43]:

$$E_{interaction} = E_{total} - (E_{surface+solution} + E_{inhibitor}) \quad (8)$$

$$E_{bindinig} = -E_{interaction} \quad (9)$$

where $E_{surface+solution}$ is assigned to the total energy of Fe (1 1 0) surface and solution without the inhibitors;$E_{inhibitor}$ indicate the total energy of inhibitors and E_{total} represents the total energy of the whole system.

3. Results and Discussion

3.1. Chemical composition.

The chemical composition found by GC/MS of the EELL shows five compounds representing 97.9%; the main constituents are palmitic acid (27.5%), then stearic acid (22.5%), and 6β-hydroxy 21-acetyloxy budesonide (22.2%). The analytical results are summarized in Table 1.

Table 1. Chemical composition of the EELL.

Index	Name of compounds	Molecular formula	Area (%)
PAL	Palmitic acid	$C_{16}H_{32}O_2$	27.5
OLE	Oleic acid	$C_{18}H_{34}O_2$	14.7
STE	Stearic acid	$C_{18}H_{36}O_2$	22.5
BUD	6β-Hydroxy 21-Acetyloxy Budesonide	$C_{27}H_{36}O_8$	22.2
HEX	1-n-Hexadecylindan	$C_{25}H_{42}$	11.0
	Total		97.9

3.2. Electrochemical measurements.

3.2.1. Potentiodynamic polarization (PDP) studies.

The mechanism of inhibition was reviewed with the aid of PDP analysis. Figure 1a introduces the polarization curves for iron dipped in a 3% NaCl medium containing various amounts of EELL. The curves were analyzed, and the polarization parameters are summarized in Table 2.

Looking at the polarization curves (Figure 1a), we observe a displacement of E_{corr} towards the cathode direction (negative direction) with a decrease of the i_{corr} caused by the increase of the EELL concentrations. It can be concluded that in the presence of EELL, the concentration of 100 ppm depicts the optimal concentration of iron in a 3% NaCl medium.

Consider Figure 1a and Table 2; it can be seen that the increase in the EELL concentration decreases the i_{corr} until reaching the minimum value 10 μA/cm^2 seen in the presence of the EELL at its optimal concentration (100 ppm), consequently of this decrease in i_{corr} the η_{PDP} increases and reaches 87.2%. This increase suggests that the molecules of the

EELL form an adsorbed layer on the iron surface, blocking the corrosion process; its effect is gradually increased with the addition of the inhibitor molecules [44].

Usually, the inhibitor can be ranked as a cathodic, anodic, or mixed inhibitor according to the deviation in E_{corr} with reference to the blank corrosive solution ($\Delta E_{corr} = E_{corr}$ (blank) - E_{corr} (with inhibitors)) [45]. Adding EELL to the 3% NaCl solutions shifts the corrosion potentials in a more negative direction compared to E_{corr}. It can be observed that the EELL inhibitor significantly blocks the cathodic reaction while it has a limited effect on the anodic reaction. Consequently, the constituents of this extract are cathode-type inhibitors with a maximum displacement reaching 176.2 mV.

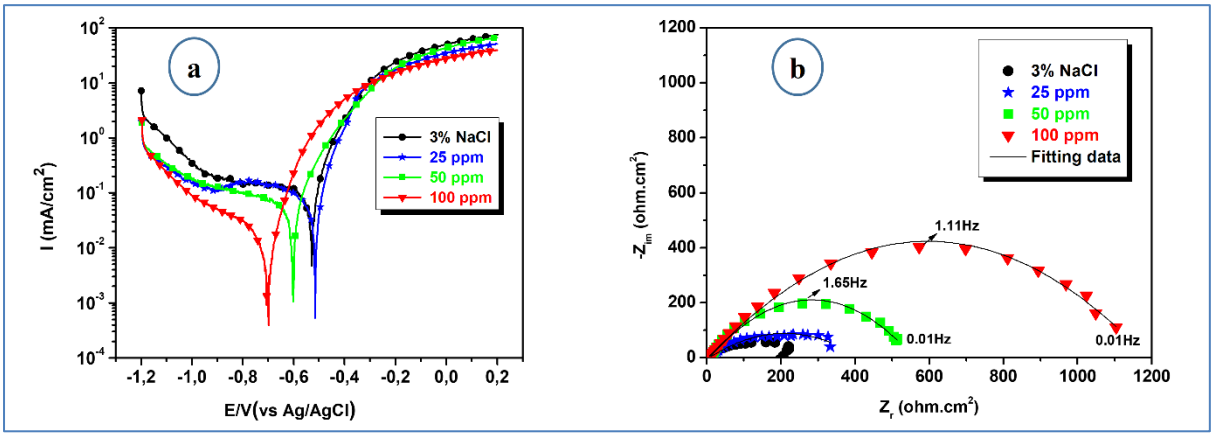

Figure 1. (a) Polarization curves and **(b)** Nyquist diagrams of the iron electrode in 3% NaCl solutions without (Blank) and with different concentrations of the EELL.

Table 2. Electrochemical parameters derived from Tafel extrapolation of the iron electrode in 3% NaCl solutions without and with various concentrations of the EELL.

	C (ppm)	$-E_{corr}$ (mV)	i_{corr} (μA/cm²)	β_a (mV)	$-\beta_c$ (mV)	η_{PDP} (%)
3% NaCl	-----	527.5 ± 2.5	78.2 ± 0.02	76.5 ± 0.03	464.4 ± 0.5	-----
EELL	25	516.6 ± 2.6	44.2 ± 0.03	66.5 ± 0.04	238.4 ± 0.5	43.4
	50	600.6 ± 3.6	32.6 ± 0.02	76.7 ± 0.02	236.3 ± 0.1	58.3
	100	703.7 ± 4.6	10.0 ± 0.01	77.1 ± 0.04	188.0 ± 0.3	87.2

3.2.2. Electrochemical impedance spectroscopy (EIS) studies.

The corrosion behavior of iron in 3% NaCl solutions with and without different concentrations of the EELL was explored by the EIS method at room temperature after immersion for 30 min.

The results of this method are represented as Nyquist plots in Figure 1b. These Nyquist plots are not absolute semicircles, phenomena attributed to the frequency dispersion of the interfacial impedance, generally due to the heterogeneity of the electrode surface. This heterogeneity can result from impurities, roughness, dislocations, adsorption of the inhibitor, and the development of the porous surface.

In the absence of the EELL inhibitor, there are two more or less well-defined loops, a capacitive loop at high frequencies and a second loop at low-frequency values. The first loop is representative of the charge transfer, and the second is assigned to the relaxation process by adsorption of a $FeOH_{ads}$ intermediate product on the metal surface [46]. In the presence of the EELL inhibitor, we note an increase in the total impedance sign of corrosion inhibition. Also, the Nyquist plots are marked by two capacitive loops. In addition, the diameter of the high-frequency loop increases with the concentration of EELL added; the bias resistance, defined by the low-frequency limit of the Nyquist plots, likewise increases. This is a sign of the

adsorption of the organic compound over the iron surface, leading to a decrease in the corrosion rate when the protective film has an appropriate thickness and shape as well.

The capacitive loops were fitted and analyzed with respect to their suitable equivalent circuit model (Figure 2), and the impedance parameters are recapitulated in Table 3. In this circuit, R_S represents the resistance of the electrolyte, R_1 is the resistance of the surface film, and Q_1 is the capacitance due to the dielectric nature of the surface film. The R_2 is the charge transfer resistance linked to the corrosion process, and Q_2 is a constant phase element (CPE) intended to replace a double layer capacity (C_{dl}) for a more proper fitting [47]. The element "n" is a coefficient that quantifies the various physical phenomena as a surface inhomogeneity resulting from the surface roughness, the adsorption of the inhibitor molecules, and the expansion of a porous layer.

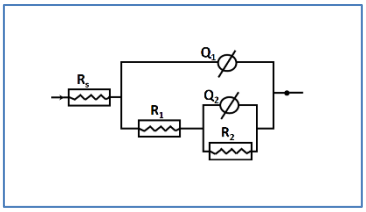

Figure 2. An electrical equivalent circuit used to model the results of impedance.

The analysis of the results grouped in Table 3 shows that in the inhibitors-free neutral chloride solution, the low R_p value obtained for the iron in the corrosive solution testifies to the metal corrosion. In the presence of the EELL inhibitor, we note a clear increase in R_p with the increase in the EELL concentration in the solution, a sign of inhibition of the corrosion process. In addition, one notices that the reduction in CPE (Q_2), which results from a local decrease in the dielectric constant and/or an increase in the thickness of the double layer, has been allocated to the development of a protective layer due to the gradual replacement of water molecules and other ions initially adsorbed over the iron surface by adsorption of inhibitor components [48].

Table 3. Electrochemical parameters derived from Nyquist plots of the iron electrode in uninhibited and inhibited 3% NaCl solutions containing different concentrations of the EELL.

	C (ppm)	$^{a}R_s$ ($\Omega.cm^2$)	$^{a}R_1$ ($\Omega.cm^2$)	$^{b}Q_1\times10^{-3}$ F $s^{(n-1)}$	$^{c}n_1$	$^{a}R_2$ ($\Omega.cm^2$)	$^{b}Q_2\times10^{-3}$ F $s^{(n-1)}$	$^{c}n_2$	$^{a}R_p$ ($\Omega.cm^2$)	η_{EIS} %
3% NaCl	Blank	7.8	87.6	1.19	0.73	128.6	6.57	0.94	216.1	-
EELL	25	11.6	124.6	0.89	0.60	207.0	0.013	0.27	331.6	34.9
	50	10.7	113.8	0.30	0.71	395.5	0.011	1.0	509.3	57.6
	100	7.9	111.8	0.20	0.70	1118	0.010	0.85	1229.8	82.4

[a]The standard deviation range for R_S, R_1 and R_2 values is between 2.5% and 5.3%.
[b]The standard deviation range for Q_1 and Q_2 values is between 0.5% and 3.4%.
[c]The standard deviation range for n values is between 0.1% and 1.5%.

3.3. Surface characterizations.

3.3.1. UV-vis analysis.

UV-vis spectra (Figure 3) were provided for the EELL before and after the iron immersion to confirm the adsorption of the inhibitor molecules on the metal substrate. The absorption spectrum related to the EELL before iron immersion presents two characteristic absorption bands, a strong band located at 210 nm, assigned to the π-π* transition resulting from the conjugated C=C bonds adsorption, and a less accentuated band centered at 264 nm, which is ascribed to n-π* electronic transition belonging to the C=O bond adsorption [49,50]. After the iron immersion in 3% NaCl containing 100 ppm EELL , it can be seen that the two

absorbance bands have been slightly shifted towards lower wavelengths (C=C from 210 to 208 nm and C=O from 268 to 264 nm). In addition, the absorbance intensity has decreased, thus confirming the adsorption of the inhibitor compounds on the iron substrate sites. These results mean that the functional groups C=C and C=O reacted with iron cations (i.e., Fe^{2+}) and thus formed complexes, which demonstrates the development of a protective film on the iron substrate [51].

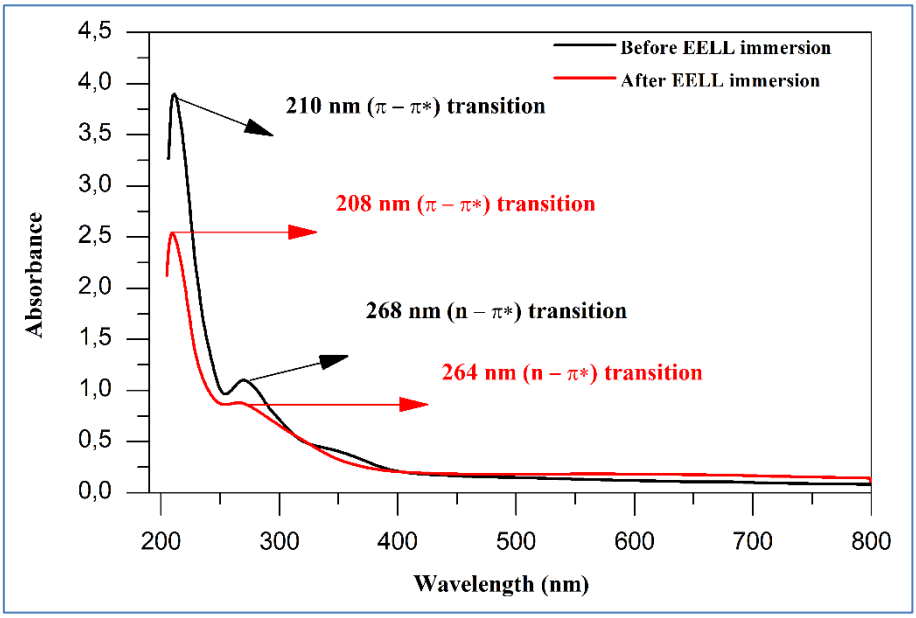

Figure 3. UV-vis spectra of the 3% NaCl solution containing 100 ppm EELL before and after iron sample immersion for 24 h.

3.3.2. FT-IR analysis.

Figure 4 shows the IR spectrum of the EELL and the corrosion product on the surface of iron dipped in the 3% NaCl solutions without 100 ppm EELL. From the IR spectrum in Figure 4(a), several bands characteristic groups of the EELL can be seen. The large band at 3432.9 cm^{-1} could be assigned to O-H groups. The bands appearing at 2920.7 and 2849.1 cm^{-1} corresponds to C-H stretching vibrations. The band at 1718.6 cm^{-1} linked to stretching vibrations of the C=O, while the C=C stretching vibrations is located at 1608.8 cm^{-1}. The band at 1024.8 cm-1 correspond to the C-O stretching vibrations. The band at 1450 cm^{-1} could be due to binding C-H in the plan, and the absorption bands at 827.1 and 765.6 cm^{-1} are characteristic of an aromatic ring.

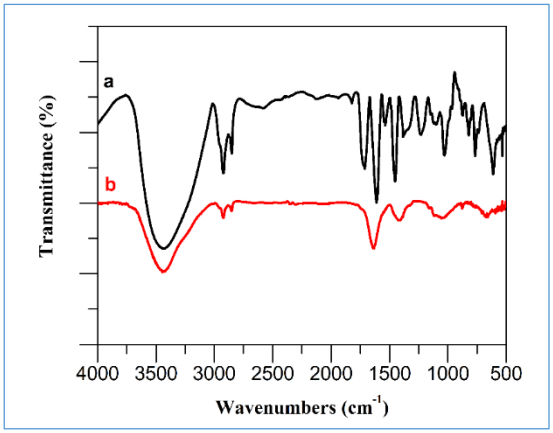

Figure 4. FTIR Spectrum **(a)** of the EELL and **(b)** the thin film formed on the iron surface immersed in 3% NaCl containing 100 ppm EELL.

On comparing Figure 4(a) and 4(b) show that an additional band has appeared at 822.1 cm^{-1} is related to the Fe-O stretching vibrations, and certain bands corresponding to the characteristic groups of EELL have shifted to higher frequency region, providing that some interaction/adsorption has been taking place over the metal surface. The –OH stretching shifted from 3432.9 to 3435.7 cm^{-1} and C=C stretching shifted from 1608.8 to 1637.4 cm^{-1} may be confirmed that there is an strong interaction between EELL and the iron surface. This shifted of the characteristic bands of the inhibitors to the higher frequency illustrates the complexation among inhibitor molecules and the iron surface.

3.3.3. Surface analysis by SEM/EDX.

The corrosion protective activity of the EELL after immersion for 24h was further analyzed using SEM/EDX techniques. SEM images and corresponding EDX spectra in the absence and presence of the EELL inhibitor are given in Figure 5. As follows from this Figure, it can be seen that the plan view of the SEM micrograph of the blank (without inhibitors) sample, which is corroded and characterized by a very rough surface with corrosion products. However, in the presence of 100 ppm EELL, the iron surface damage was strongly reduced, and the iron sample appeared smooth. This observation between the inhibited and uninhibited deduced the formation of a protective barrier layer on the iron surface due to the adsorption of active compounds of the EELL on the iron surface. Also, EDX was used to determine the elements present on the iron surface without and with 100 ppm EELL.

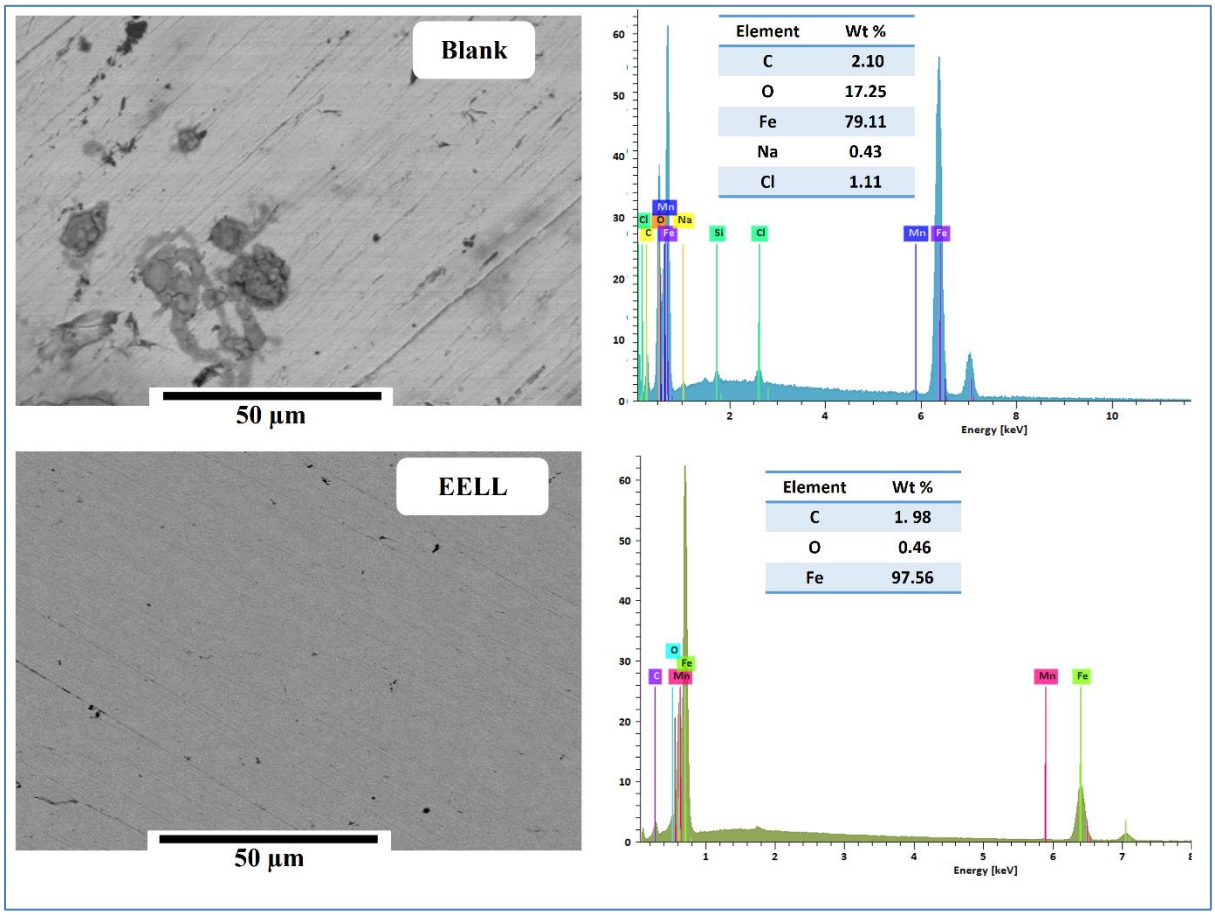

Figure 5. SEM/EDX micrographs of iron after immersion for 24h in 3% NaCl solution without (Blank) and with 100 ppm EELL.

According to Figure 5, in the absence of the EELL (blank), the spectra contained mainly the characteristic peaks of C, O, and Fe with amounts around 2.10, 17.25, and 79.11 (wt %),

respectively. This suggested the formation of metal oxides/hydroxides and chlorides as corrosion products on the iron surface. In the presence of 100 ppm EELL, we remarked the reduction in peak intensity which the percentage of O to 0.46 (wt %). Hence, we could say that the molecules. EELL adsorbed on the iron surface, preventing the formation of oxides/hydroxides and chlorides. In addition, the Fe (wt %) increases shifted to 97.56 (wt %) because it is related to the adsorption of the inhibitors on the iron surface, leading to the development of a protective film. It has been found that there is a good match between the SEM micrograph and the EDX data.

3.4. Theoretical investigations.

3.4.1. Global quantum chemical descriptors.

The DFT is one of the most useful methods to analyze the inhibitor/surface interactions; the E_{HOMO} and E_{LUMO} orbitals are two descriptors that can be employed to explain corrosion inhibition efficiency. The more the energy gap between the LUMO and the HOMO orbitals decreases, the more the corrosion inhibition ability of inhibitors increases. The results of Table 4 show that the BUD inhibitor presents a high E_{HOMO} (-6.899 eV) and a low E_{LUMO} (-1.840 eV), which reflect its ability to give and accept the electrons. Therefore its adsorption capacity on the metal surface. The BUD and HEX inhibitors, which present the low energies gaps, show in Figure 6 that molecular electron density is located around the 2,5-Cyclohexadienone and Indane group, respectively. These groups can explain the ability of electron-hole transport and the corrosion inhibition efficiency between the iron metal and the mentioned inhibitors (BUD and HEX). For PAL and STE compounds, the low E_{HOMO} and high E_{LUMO} values could increase their abilities to accept electrons and therefore decrease the corrosion inhibition efficiency; despite this, the electron density located around the carboxyl group could give electrons to the metal surface (see Figure 6).

The electronics indices such as electronegativity (χ), hardness (η), nucleophilicity (N), softness (σ), and electrophilicity (ω) could also be used to discuss the corrosion inhibition interactions. The inhibitors with high electronegativity, nucleophilicity, and softness values are very reactive with the metal surface of the iron. In contrast, the inhibitors with high electrophilicity and global hardness values are resistant to charge transfer.

Table 4 shows that the BUD inhibitor presents higher electronegativity (χ = 4.369) and nucleophilicity (N = 2.469), which indicate its ability to inhibit iron corrosion. Moreover, the high values of electrons transferred parameters (ΔN = 0.225) of OLE inhibitor, and HEX (ΔN = 0.221) show the ability of these compounds on the corrosion inhibition observed experimentally. The PAL and STE inhibitors are electroatracting compounds with high global hardness values (η = 3.912 and 3.910), which decrease their inhibition abilities. These results suggest that the two molecules BUD and HEX are more likely to explain the reactivity of the corrosion inhibition observed experimentally.

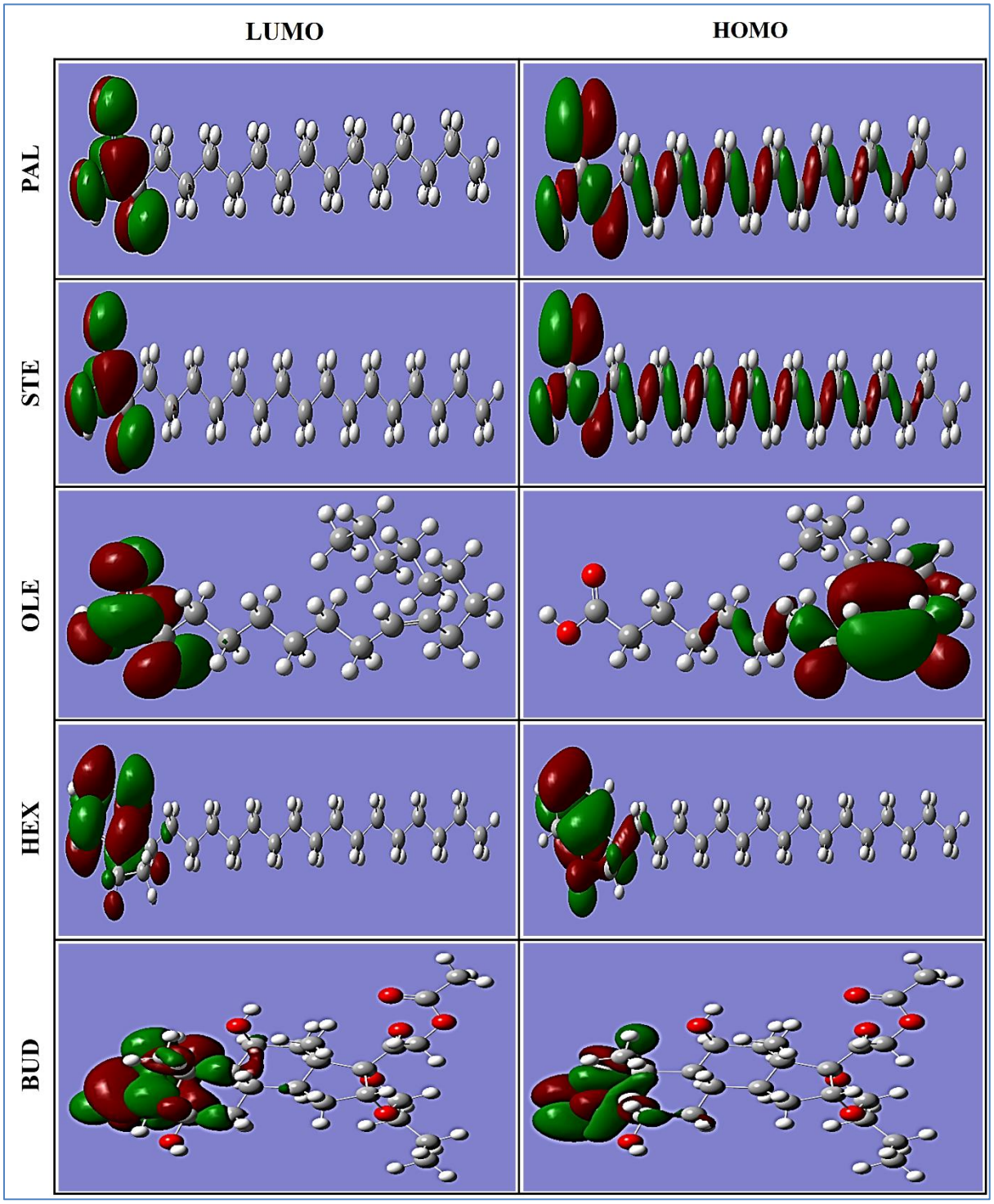

Figure 6. DFT-derived Frontier molecular orbital density distribution: LUMO and HOMO of PAL, STE, OLE, HEX, and BUD compounds.

Table 4. Calculated quantum chemical parameters of studied EELL compounds calculated at the B3LYP with 6-311G** basis.

Inhibitors name	E_{LUMO} (eV)	E_{HOMO} (eV)	ΔE_{gap} (eV)	I_p (eV)	E_A (eV)	χ (eV)	η (eV)	ω (eV)	N (eV)	σ $(eV)^{-1}$	ΔN
PAL	0.043	-7.781	7.824	7.781	-0.043	3.869	3.912	1.956	1.587	0.256	0.122
STE	0.043	-7.778	7.821	7.778	-0.043	3.867	3.910	1.955	1.590	0.256	0.122
OLE	0.054	-6.672	6.726	6.672	-0.054	3.309	3.363	1.681	2.696	0.297	0.225
HEX	-0.382	-6.540	6.158	6.540	0.382	3.461	3.079	1.540	2.828	0.325	0.221
BUD	-1.840	-6.899	5.059	6.899	1.840	4.369	2.529	1.565	2.469	0.395	0.089

3.4.2. Molecular dynamics simulations.

In recent years, through MD simulations, it has been feasible to gain further deep insight into the mode in which the green inhibitors adsorb and how much change in an inhibitor would constitute a significant difference in corrosion inhibition. Therefore, the MD process was performed until the system's temperature and energy were balanced and the whole system reached equilibrium. Table 5 depicts the interaction energy ($E_{interaction}$), and binding energy ($E_{binding}$) values obtained, while Figure 7 shows the side and top views of low-energy adsorption configurations of the five inhibitor molecules onto the Fe (110) surface. These inhibitor molecules possess potential binding sites, as shown in the results from the GQCDs.

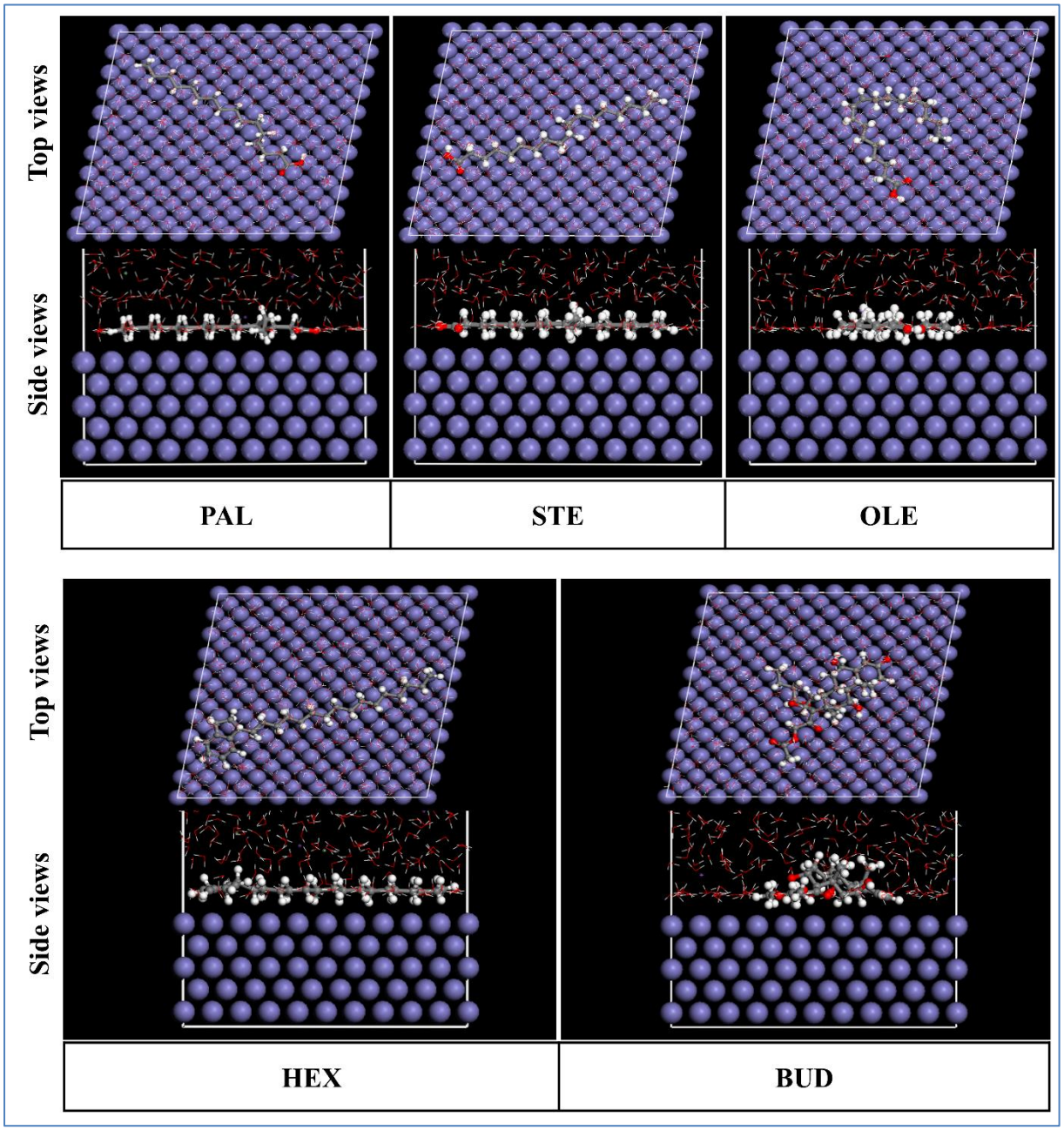

Figure 7. (a) Side and **(b)** Top views of the most stable configurations for the adsorption of PAL, STE, OLE, HEX, and BUD compounds over Fe (110) surface obtained from MD simulations.

The adsorption centers of the studied inhibitors on the Fe (110) surface belong to the oxygen heteroatoms and π systems of aromatic rings; the compounds show almost parallel or flat orientations on the iron surface to maximize surface contact, which ensures a large surface

area to inhibit the dissolution of the metal surface. The strength of inhibitors adsorbed on the iron surface may be expressed in terms of their interaction energies (Einteraction) on the iron surface.

The negative values obtained for the Einteraction denote that the inhibitors studied adsorb spontaneously on the Fe surface (110). The lower the interaction energy, the adequate inhibitor-surface interaction and, thus, the better the corrosion inhibition performance. The order of decrease in interaction energy is BUD (-1134,9 kcal/mol) < HEX (-1051,4 kcal/mol) < STE (-967.07 kcal/mol) < OLE (-924,24 kcal/mol) < PAR (-886,63 kcal/mol). Based on the present values, BUD and HEX possess the highest binding energies, and therefore they present a better inhibiting property for the iron surface. The adsorption of these inhibitor molecules over the surface of Fe (110) this fact by sharing electrons between the heteroatoms and p systems in the inhibitors and the active surface sites of this metal (Fe (110)). This allows the possibility of a bond formation (π-π) resulting from the overlap of the free doublet of oxygen atoms and carbon-carbon pi-orbitals in inhibitors and the electrons (3d) of the iron atoms.

It should be noted that the same trend is observed with respect to quantum chemical descriptors that produce results consistent with corrosion inhibition performance. Altogether, results from these computational studies confirm the inhibition efficiencies reported in experimental results. The interaction energies of the negative value of five inhibitors shown in Table 5 again indicate the ability of these molecules to bind to the metal surface and, in that contact, construct together an anticorrosive film over the iron surface.

Table 5 Interaction and binding energies obtained from MD simulation of the EELL compounds adsorbed on Fe (110) surface.

Simulations models	$E_{interaction}$ (KJ/mol)	$E_{binding}$ (KJ/mol)
Fe (110) + 500 H_2O + 5 NaCl + PAR	-886.63	886.63
Fe (110) + 500 H_2O + 5 NaCl + STE	-967.07	967.07
Fe (110) + 500 H_2O + 5 NaCl + OLE	-924.24	924.24
Fe (110) + 500 H_2O + 5 NaCl + HEX	-1051.4	1051.4
Fe (110) + 500 H_2O + 5 NaCl + BUD	-1134.9	1134.9

4. Conclusions

The theoretical and experimental investigations of the corrosion inhibition of Lentisk leaf extract as an effective green inhibitor on the iron in 3% NaCl solution were performed via electrochemical techniques and surface analyses. Electrochemical measurements (EIS and PDP) results demonstrated that inhibition efficiency increases with improving EELL concentration, achieving the highest value at 100 ppm. We also deduce that EELL is a cathodic-type inhibitor. The corrosion product over the iron surface in the presence of the EELL inhibitor characterized by UV-Vis, FT-IR, and SEM-EDX spectra may conform to the complex film formed between the metal and the active groups present in the EELL. In addition to the experimental findings, theoretical studies, including molecular dynamics and quantum mechanics simulations, revealed that the reactive sites of the components EELL with the corrosion inhibition abilities have a great tendency to adsorb on the iron surface, and all the outcomes showed significant correlations with each other. Summing up the results, it can be concluded by combining experiments and theoretical calculations that the EELL has the potential to be developed as an eco-friendly inhibitor for iron corrosion.

Funding

This research received no external funding.

Acknowledgments

This research has no acknowledgment.

Conflicts of Interest

The authors declare no conflict of interest.

References

1. Al-Moubaraki, A.H.; Obot, I.B. Corrosion challenges in petroleum refinery operations: Sources, mechanisms, mitigation, and future outlook. *J. Saudi Chem. Soc.* **2021**, *25*, 101370, https://doi.org/10.1016/j.jscs.2021.101370.
2. Majd, M.T.; Asaldoust, S.; Bahlakeh, G.; Ramezanzadeh, B.; Ramezanzadeh, M. Green method of carbon steel effective corrosion mitigation in 1 M HCl medium protected by *Primula vulgaris* flower aqueous extract via experimental, atomic-level MC/MD simulation and electronic-level DFT theoretical elucidation. *J. Mol. Liq.* **2019**, *284*, 658–674, https://doi.org/10.1016/j.molliq.2019.04.037.
3. Sanaei, Z.; Ramezanzadeh, M.; Bahlakeh, G.; Ramezanzadeh, B. Use of *Rosa canina* fruit extract as a green corrosion inhibitor for mild steel in 1 M HCl solution: A complementary experimental, molecular dynamics and quantum mechanics investigation. *J. Ind. Eng. Chem.* **2019**, *69*, 18–31, https://doi.org/10.1016/j.jiec.2018.09.013.
4. Kumari, P.; Lavanya, M. Plant extracts as corrosion inhibitors for aluminum alloy in NaCl environment - recent review. *J. Chil. Chem. Soc.* **2022**, *67*, 5490–5495, https://doi.org/10.4067/s0717-97072022000205490.
5. Macedo, R.G.M. de A.; Marques, N. do N.; Tonholo, J.; Balaban, R. de C. Water-soluble carboxymethylchitosan used as corrosion inhibitor for carbon steel in saline medium. *Carbohydr. Polym.* **2019**, *205*, 371–376, https://doi.org/10.1016/j.carbpol.2018.10.081.
6. Miralrio, A.; Vázquez, A.E. Plant extracts as green corrosion inhibitors for different metal surfaces and corrosive media: A review. *Processes* **2020**, *8*, 1–27, https://doi.org/10.3390/PR8080942.
7. Barbouchi, M.; Benzidia, B.; Aouidate, A.; Ghaleb, A.; El Idrissi, M.; Choukrad, M. Theoretical modeling and experimental studies of Terebinth extracts as green corrosion inhibitor for iron in 3 % NaCl medium. *J. King Saud Univ. - Sci.* **2020**, *32*, 2995–3004, https://doi.org/10.1016/j.jksus.2020.08.004.
8. Bhardwaj, N.; Sharma, P.; Kumar, V. *Triticum aestivum* extract as corrosion inhibitor for stainless steel (SS-410) in acidic media: Experimental and theoretical study. *Curr. Res. Green Sustain. Chem.* **2021**, *4*, 100189, https://doi.org/10.1016/j.crgsc.2021.100189.
9. Hossain, N.; Chowdhury, M.A.; Iqbal, A.K.M.P.; Islam, M.S.; Sheikh Omar, N.Y.; Saifullah, A.Z.A. *Paederia Foetida* leaves extract as a green corrosion inhibitor for mild steel in hydrochloric acid solution. *Curr. Res. Green Sustain. Chem.* **2021**, *4*, 100191, https://doi.org/10.1016/j.crgsc.2021.100191.
10. Eddy, N.O.; Ibok, U.J.; Garg, R.; Garg, R.; Iqbal, A.; Amin, M.; Mustafa, F.; Egilmez, M.; Galal, A.M. A Brief Review on Fruit and Vegetable Extracts as Corrosion Inhibitors in Acidic Environments. *Molecules* **2022**, *27*, 2991, https://doi.org/10.3390/molecules27092991.
11. Benzidia, B.; Barbouchi, M.; Hsissou, R.; Zouarhi, M.; Erramli, H.; Hajjaji, N. A combined experimental and theoretical study of green corrosion inhibition of bronze B66 in 3% NaCl solution by *Aloe saponaria* (syn. Aloe maculata) tannin extract. *Curr. Res. Green Sustain. Chem.* **2022**, *5*, 100299, https://doi.org/10.1016/j.crgsc.2022.100299.
12. Wang, Q.; Zheng, H.; Liu, L.; Zhang, Q.; Wu, X.; Yan, Z.; Sun, Y.; Li, X. Insight into the anti–corrosion behavior of *Reineckia Carnea* leaves extract as an eco–friendly and high–efficiency corrosion inhibitor. *Ind. Crops Prod.* **2022**, *188*, 115640, https://doi.org/10.1016/j.indcrop.2022.115640.
13. Elqars, E.; Guennoun, M.; Sqali Houssini, N.; Thoume, A.; Mechnou, I.; Essadki, A.; Nbigui, T. The Adsorption Performance of Chicken Excrement Extract as Corrosion Inhibition of Carbon Steel in a 1 M HCl Medium. *J. Bio- Tribo-Corrosion* **2021**, *7*, 1–12, https://doi.org/10.1007/s40735-021-00520-9.
14. Zakeri, A.; Bahmani, E.; Aghdam, A.S.R. Plant extracts as sustainable and green corrosion inhibitors for protection of ferrous metals in corrosive media: A mini review. *Corros. Commun.* **2022**, *5*, 25–38, https://doi.org/10.1016/j.corcom.2022.03.002.
15. Kusumaningrum, I.; Soenoko, R.; Siswanto, E.; Gapsari, F. Investigation of *Artocarpus Heteropyllus* peel extract as non-toxic corrosion inhibitor for pure copper protection in nitric acid. *Case Stud. Chem. Environ. Eng.* **2022**, *6*, 100223, https://doi.org/10.1016/j.cscee.2022.100223.
16. Xu, C.; Tan, B.; Zhang, S.; Li, W. Corrosion inhibition of copper in sulfuric acid by *Leonurus japonicus*

Houtt. extract as a green corrosion inhibitor: Combination of experimental and theoretical research. *J. Taiwan Inst. Chem. Eng.* **2022**, *139*, 104532, https://doi.org/10.1016/j.jtice.2022.104532.
17. Prifiharni, S.; Mashanafie, G.; Priyotomo, G.; Royani, A.; Ridhova, A.; Elya, B.; Soedarsono, J.W. Extract sarampa wood (*Xylocarpus Moluccensis*) as an eco-friendly corrosion inhibitor for mild steel in HCl 1M. *J. Indian Chem. Soc.* **2022**, *99*, 100520, https://doi.org/10.1016/j.jics.2022.100520.
18. Shang, Z.; Zhu, J. Overview on plant extracts as green corrosion inhibitors in the oil and gas fields. *J. Mater. Res. Technol.* **2021**, *15*, 5078–5094, https://doi.org/10.1016/j.jmrt.2021.10.095.
19. Haddadi, S.A.; Alibakhshi, E.; Bahlakeh, G.; Ramezanzadeh, B.; Mahdavian, M. A detailed atomic level computational and electrochemical exploration of the *Juglans regia* green fruit shell extract as a sustainable and highly efficient green corrosion inhibitor for mild steel in 3.5 wt% NaCl solution. *J. Mol. Liq.* **2019**, *284*, 682–699, https://doi.org/10.1016/j.molliq.2019.04.045.
20. Landau, S.; Muklada, H.; Markovics, A.; Azaizeh, H. Traditional Uses of *Pistacia lentiscus* in Veterinary and Human Medicine. In *Medicinal and Aromatic Plants of the World*; Yavin, Z., Dudai, N., Eds.; Springer Netherlands, 2014; pp. 163–180 ISBN 9789401792752, https://link.springer.com/chapter/10.1007/978-94-017-9276-9_8.
21. Pachi, V.K.; Mikropoulou, E. V.; Gkiouvetidis, P.; Siafakas, K.; Argyropoulou, A.; Angelis, A.; Mitakou, S.; Halabalaki, M. Traditional uses, phytochemistry and pharmacology of Chios mastic gum (*Pistacia lentiscus* var. Chia, Anacardiaceae): A review. *J. Ethnopharmacol.* **2020**, *254*, 112485, https://doi.org/10.1016/j.jep.2019.112485.
22. Milia, E.; Bullitta, S.M.; Mastandrea, G.; Szotáková, B.; Schoubben, A.; Langhansová, L.; Quartu, M.; Bortone, A.; Eick, S. Leaves and fruits preparations of *Pistacia lentiscus* L.: A review on the ethnopharmacological uses and implications in inflammation and infection. *Antibiotics* **2021**, *10*, 425, https://doi.org/10.3390/antibiotics10040425.
23. Botsaris, G.; Orphanides, A.; Yiannakou, E.; Gekas, V.; Goulas, V. Antioxidant and antimicrobial Effects of *Pistacia lentiscus* L. extracts in pork sausages. *Food Technol. Biotechnol.* **2015**, *53*, 472–478, https://doi.org/10.17113/ftb.53.04.15.4051.
24. Bouyahya, A.; Chadon Assemian, I.C.; Mouzount, H.; Bourais, I.; Et-Touys, A.; Fellah, H.; Benjouad, A.; Dakka, N.; Bakri, Y. Could volatile compounds from leaves and fruits of *Pistacia lentiscus* constitute a novel source of anticancer, antioxidant, antiparasitic and antibacterial drugs? *Ind. Crops Prod.* **2019**, *128*, 62–69, https://doi.org/10.1016/j.indcrop.2018.11.001.
25. Aissi, O.; Boussaid, M.; Messaoud, C. Essential oil composition in natural populations of *Pistacia lentiscus* L. from Tunisia: Effect of ecological factors and incidence on antioxidant and antiacetylcholinesterase activities. *Ind. Crops Prod.* **2016**, *91*, 56–65, https://doi.org/10.1016/j.indcrop.2016.06.025.
26. Yosr, Z.; Imen, B.H.Y.; Rym, J.; Chokri, M.; Mohamed, B. Sex-related differences in essential oil composition, phenol contents and antioxidant activity of aerial parts in *Pistacia lentiscus* L. during seasons. *Ind. Crops Prod.* **2018**, *121*, 151–159, https://doi.org/10.1016/j.indcrop.2018.04.067.
27. Barbouchi, M.; Elamrani, K.; Idrissi, M. El; Choukrad, M. A comparative study on phytochemical screening , quantification of phenolic contents and antioxidant properties of different solvent extracts from various parts of *Pistacia lentiscus* L. *J. King Saud Univ. - Sci.* **2020**, *32*, 302–306, https://doi.org/10.1016/j.jksus.2018.05.010.
28. Abed, A.; Rachid, D.; Catherine, M.; Ismahene, S.; Nadia, B.; Hichem, D.; Charef, R.; Mehdi, E.; Farida, T.; Mounira, O.K.; et al. Chemical composition and antibacterial activity of essential oilfrom leaves and twigs of *Pistacia lentiscus* growing in Mostaganem Province (Algeria). *Int. J. Biosci.* **2017**, *10*, 146–158, https://doi.org/10.12692/ijb/10.5.146-158.
29. Catalani, S.; Palma, F.; Battistelli, S.; Benedetti, S. Oxidative stress and apoptosis induction in human thyroid carcinoma cells exposed to the essential oil from *Pistacia lentiscus* aerial parts. *PLoS One* **2017**, *12*, 1–15, https://doi.org/10.1371/journal.pone.0172138.
30. Remila, S.; Atmani-Kilani, D.; Delemasure, S.; Connat, J.L.; Azib, L.; Richard, T.; Atmani, D. Antioxidant, cytoprotective, anti-inflammatory and anticancer activities of *Pistacia lentiscus* (Anacardiaceae) leaf and fruit extracts. *Eur. J. Integr. Med.* **2015**, *7*, 274–286, https://doi.org/10.1016/j.eujim.2015.03.009.
31. Barra, A.; Coroneo, V.; Dessi, S.; Cabras, P.; Angioni, A. Characterization of the Volatile Constituents in the Essential Oil of *Pistacia lentiscus* L . from Different Origins and Its Antifungal and Antioxidant Activity. *J. Agric. Food Chem* **2007**, *55*, 7093−7098, https://doi.org/10.1021/jf071129w.
32. Kordali, S.; Cakir, A.; Zengin, H.; Duru, M.E. Antifungal activities of the leaves of three *Pistacia species* grown in Turkey. *Fitoterapia* **2003**, *74*, 164–167, https://doi.org/10.1016/S0367-326X(02)00320-9.
33. Buriani, A.; Fortinguerra, S.; Sorrenti, V.; Dall'Acqua, S.; Innocenti, G.; Montopoli, M.; Gabbia, D.; Carrara, M. Human adenocarcinoma cell line sensitivity to essential oil phytocomplexes from *Pistacia* species: A multivariate approach†. *Molecules* **2017**, *22*, https://doi.org/10.3390/molecules22081336.
34. Mehenni, C.; Atmani-Kilani, D.; Dumarçay, S.; Perrin, D.; Gérardin, P.; Atmani, D. Hepatoprotective and antidiabetic effects of *Pistacia lentiscus* leaf and fruit extracts. *J. Food Drug Anal.* **2016**, *24*, 653–669, https://doi.org/10.1016/j.jfda.2016.03.002.
35. Benzidia, B.; Barbouchi, M.; Hammouch, H.; Belahbib, N.; Zouarhi, M.; Erramli, H.; Ait Daoud, N.; Badrane, N.; Hajjaji, N. Chemical composition and antioxidant activity of tannins extract from green rind of *Aloe vera*

(L.) Burm. F. *J. King Saud Univ. - Sci.* **2019**, *31*, 1175–1181, https://doi.org/10.1016/j.jksus.2018.05.022.
36. Barbouchi, M.; Benzidia, B.; Choukrad, M. Chemical variability in essential oils isolated from roots, stems, leaves and flowers of three *Ruta* species growing in Morocco. *J. King Saud Univ. - Sci.* **2021**, *33*, 101634, https://doi.org/10.1016/j.jksus.2021.101634.
37. Domingo, L.R.; Ríos-Gutiérrez, M.; Pérez, P. Applications of the conceptual density functional theory indices to organic chemistry reactivity. *Molecules* **2016**, *21*, 1–22, https://doi.org/10.3390/molecules21060748.
38. Abdallah, M.; El Guesmi, N.; Al-Gorair, A.S.; El-Sayed, R.; Meshabi, A.; Sobhi, M. Enhancing the anticorrosion performance of mild steel in sulfuric acid using synthetic non-ionic surfactants: practical and theoretical studies. *Green Chem. Lett. Rev.* **2021**, *14*, 381–393, https://doi.org/10.1080/17518253.2021.1921858.
39. Galai, M.; Rbaa, M.; Ouakki, M.; Abousalem, A.S.; Ech-chihbi, E.; Dahmani, K.; Dkhireche, N.; Lakhrissi, B.; EbnTouhami, M. Chemically functionalized of 8-hydroxyquinoline derivatives as efficient corrosion inhibition for steel in 1.0 M HCl solution: Experimental and theoretical studies. *Surfaces and Interfaces* **2020**, *21*, 100695, https://doi.org/10.1016/j.surfin.2020.100695.
40. Obot, I.B.; Macdonald, D.D.; Gasem, Z.M. Density functional theory (DFT) as a powerful tool for designing new organic corrosion inhibitors: Part 1: An overview. *Corros. Sci.* **2015**, *99*, 1–30, https://doi.org/10.1016/j.corsci.2015.01.037.
41. Sun, H. COMPASS: An ab Initio Force-Field Optimized for Condensed-Phase ApplicationsOverview with Details on Alkane and Benzene Compounds. *J. Phys. Chem. B* **1998**, https://doi.org/10.1021/jp980939v.
42. Hsissou, R.; Abbout, S.; Seghiri, R.; Rehioui, M.; Berisha, A.; Erramli, H.; Assouag, M.; Elharfi, A. Evaluation of corrosion inhibition performance of phosphorus polymer for carbon steel in [1 M] HCl: Computational studies (DFT, MC and MD simulations). *J. Mater. Res. Technol.* **2020**, *9*, 2691–2703, https://doi.org/10.1016/j.jmrt.2020.01.002.
43. Hsissou, R.; Abbout, S.; Benhiba, F.; Seghiri, R.; Safi, Z.; Kaya, S.; Briche, S.; Serdaroğlu, G.; Erramli, H.; Elbachiri, A.; et al. Insight into the corrosion inhibition of novel macromolecular epoxy resin as highly efficient inhibitor for carbon steel in acidic mediums: Synthesis, characterization, electrochemical techniques, AFM/UV–Visible and computational investigations. *J. Mol. Liq.* **2021**, *337*, https://doi.org/10.1016/j.molliq.2021.116492.
44. Muzakir, M.M.; Nwosu, F.O.; Amusat, S.O. Mild Steel Corrosion Inhibition in a NaCl Solution by Lignin Extract of *Chromolaena odorata*. **2019**, *37*, 359–372, https://doi.org/10.4152/pea.201906359.
45. Pradityana, A.; Shahab, A.; Noerochim, L.; Susanti, D. Inhibition of Corrosion of Carbon Steel in 3 . 5 % NaCl Solution by *Myrmecodia Pendans* Extract. *Int. J. Corros.* **2016**, *2016*, 1–6, https://doi.org/10.1155/2016/6058286.
46. Xu, W.; Han, E.H.; Wang, Z. Effect of tannic acid on corrosion behavior of carbon steel in NaCl solution. *J. Mater. Sci. Technol.* **2019**, *35*, 64–75, https://doi.org/10.1016/j.jmst.2018.09.001.
47. Deng, S.; Li, X.; Xie, X. Hydroxymethyl urea and 1,3-bis(hydroxymethyl) urea as corrosion inhibitors for steel in HCl solution. *Corros. Sci.* **2014**, *80*, 276–289, https://doi.org/10.1016/j.corsci.2013.11.041.
48. Bentiss, F.; Gassama, F.; Barbry, D.; Gengembre, L.; Vezin, H.; Lagrenée, M.; Traisnel, M. Enhanced corrosion resistance of mild steel in molar hydrochloric acid solution by 1,4-bis(2-pyridyl)-5H-pyridazino[4,5-b]indole: Electrochemical, theoretical and XPS studies. *Appl. Surf. Sci.* **2006**, *252*, 2684–2691, https://doi.org/10.1016/j.apsusc.2005.03.231.
49. Motamedi, M.; Ramezanzadeh, B.; Mahdavian, M. Corrosion inhibition properties of a green hybrid pigment based on Pr-*Urtica Dioica* plant extract. *J. Ind. Eng. Chem.* **2018**, *66*, 116–125, https://doi.org/10.1016/j.jiec.2018.05.021.
50. Salehi, E.; Naderi, R.; Ramezanzadeh, B. Synthesis and characterization of an effective organic/inorganic hybrid green corrosion inhibitive complex based on zinc acetate/*Urtica Dioica*. *Appl. Surf. Sci.* **2017**, *396*, 1499–1514, https://doi.org/10.1016/j.apsusc.2016.11.198.
51. Dehghani, A.; Bahlakeh, G.; Ramezanzadeh, B.; Ramezanzadeh, M. Integrated modeling and electrochemical study of Myrobalan extract for mild steel corrosion retardation in acidizing media. *J. Mol. Liq.* **2020**, *298*, 112046, https://doi.org/10.1016/j.molliq.2019.112046.